
CONTOUR FIELD BASED ELLIPTICAL SHAPE PRIOR FOR THE SEGMENT ANYTHING MODEL

A PREPRINT

Xinyu Zhao, Jun Liu*, Faqiang Wang†, Li Cui, and Yuping Duan
Laboratory of Mathematics and Complex Systems (Ministry of Education of China),
School of Mathematical Sciences, Beijing Normal University, Beijing, 100875, China.

ABSTRACT

The elliptical shape prior information plays a vital role in improving the accuracy of image segmentation for specific tasks in medical and natural images. Existing deep learning-based segmentation methods, including the Segment Anything Model (SAM), often struggle to produce segmentation results with elliptical shapes efficiently. This paper proposes a new approach to integrate the prior of elliptical shapes into the deep learning-based SAM image segmentation techniques using variational methods. The proposed method establishes a parameterized elliptical contour field, which constrains the segmentation results to align with predefined elliptical contours. Utilizing the dual algorithm, the model seamlessly integrates image features with elliptical priors and spatial regularization priors, thereby greatly enhancing segmentation accuracy. By decomposing SAM into four mathematical sub-problems, we integrate the variational ellipse prior to design a new SAM network structure, ensuring that the segmentation output of SAM consists of elliptical regions. Experimental results on some specific image datasets demonstrate an improvement over the original SAM.

Keywords Image segmentation · Elliptical shape · Soft threshold dynamics · Duality

1 Introduction

Image segmentation is an essential branch of computer vision with widespread applications in fields such as medical diagnosis, autonomous driving, and remote sensing. With the rapid advancements in computer vision and machine learning technologies, image segmentation methods have exhibited diverse and sophisticated trends. Currently, mainstream approaches to image segmentation generally fall into two categories: variational models and deep learning-based models. Variational models, such as the Potts model (Potts, 1952), active contour models (Kass et al., 1987; Chan and Vese, 2001), and graph cut (Boykov and Jolly, 2001), typically achieve image segmentation by minimizing an energy function. This energy function usually comprises two components: a fidelity term, which measures the similarity or dissimilarity between different regions in the image, and a regularization term, which helps maintain the spatial continuity and structural coherence within the segmentation results.

To further enhance the accuracy and stability of image segmentation, many variational models integrate spatial prior information. These spatial priors encompass spatial regularization, region volumes, region shapes, and domain-specific knowledge. For instance, Das and Veksler (Das et al., 2009) defined a non-rotationally invariant compact prior with respect to the horizontal and vertical axes. In (Vicente et al., 2008), a connectivity constraint was proposed, mandating that the pixel points provided by users must be connected to the segmented object. Vicente (Veksler, 2008) proposed a star-shaped prior term, which requires that every pixel x on the line connecting the center c and any pixel y in the foreground lies within the foreground. Gorelick *et al.* (Gorelick et al., 2017) penalized all 1-0-1 configurations along the lines in the segmented region to constrain the convexity of the region. In paper (Yan et al., 2020), a convexity constraint was expressed using the gradient of signed distance functions and integrated into the active contour model. While

*Corresponding authors.

†Corresponding authors.

the convex prior is helpful for image segmentation in some fields, it is not specific enough for the task of segmenting elliptical objects.

Segmentation of circular and elliptical shapes in images presents a ubiquitous challenge across diverse domains. For instance, within medical imaging, cell nuclei and optic cups commonly display elliptical forms. Wu *et al.* (Wu et al., 1998) proposed an elliptical parameter fitting algorithm for segmenting cell images, which, to our knowledge, was the earliest attempt to integrate elliptical priors into image segmentation. This method used the image information to construct an elliptical grayscale image to approximate the original image, which was susceptible to the influence of image noise and uneven textures. Additionally, an elliptic function was integrated into the dissimilarity metric of FCM clustering by Leung *et al.* (Leung et al., 2004) for lip image segmentation. Subsequently, in (Slabaugh and Unal, 2005), the difference between the segmentation result and the reference ellipse mask was incorporated into the energy function of the graph cut method. This approach requires fitting the best ellipse during the iterative process to update the shape prior term, resulting in high computational costs.

In (Verma et al., 2014; Ukpai et al., 2014), authors incorporated an elliptical shape prior into the parameter active contour model. Moreover, in (Wu et al., 2013), a circular energy function was integrated into the snake model for endocardium extraction. While shape prior active contour methods can enhance segmentation accuracy, they often suffer from numerical instability and are susceptible to getting trapped in local minima.

Compared to learning-based models, variational models excel in integrating spatial prior information. However, the similarity measure in variational models is typically based on manually selected low-level image features, like grayscale intensity, color, and edges. When faced with a substantial number of supervised samples, variational models may not efficiently extract complex deep features compared to learning-based models like FCN (Shelhamer et al., 2017) or U-Net (Ronneberger et al., 2015). However, for certain specific segmentation tasks, the available datasets are limited. In response to this challenge, researchers in recent years have been dedicated to developing universal image segmentation models, such as the Segment Anything Model (SAM) (Kirillov et al., 2023). Essentially, SAM is a promptable image segmentation model capable of accurately segmenting targets when provided with points, boxes, or text cues. SAM demonstrates robust generalization capabilities. Existing studies have successfully applied the SAM to challenging tasks (Ma et al., 2024; Hu et al., 2023; Cheng et al., 2023; Qiu et al., 2023; Zhang et al., 2024). To our knowledge, most studies apply SAM to downstream tasks by adding adapters to the network structure (Qiu et al., 2023; Zhang et al., 2024; Chen et al., 2023), which lacks a clear mathematical basis. Due to repetitive attention layers and upsampling/downsampling in the network architecture, spatial positional information in images may be compromised, making it challenging to satisfy basic segmentation requirements like spatial smoothness and shape constraints. This defect is also common in general deep neural networks.

There are primarily three strategies for incorporating specific spatial information into the network. First, the post-processing method integrates the output features of the network into the variational model. Although this approach can improve segmentation performance to some extent, the post-processing results cannot be backpropagated during model training. Second, modifying the loss function of neural networks by introducing regularization terms can enhance network performance. Mirikharaji and Hamarneh (Mirikharaji and Hamarneh, 2018) incorporated a star-shaped prior term into the cross-entropy loss. A convex shape prior term was integrated into the loss function by Han *et al.* (Han et al., 2020). Akinlar *et al.* (Akinlar et al., 2022) incorporated the average distance between the ground truth pupil ellipse and the detected pupil boundary as a shape prior regularization term within the loss function. However, these methods are highly sensitive to input data in the prediction since the prediction phase does not involve the loss function. Lastly, the third strategy involves unfolding the variational segmentation algorithm into corresponding modules integrated into the network structure, combining the advantages of both post-processing and loss function methods. For example, Liu *et al.* (Liu et al., 2022) introduced a soft thresholding dynamic (STD) into the softmax activation function, which endows the outputs of DCNNs with specific priors such as spatial regularization, volume preservation, and star-shaped priors.

In this study, we propose a novel elliptical shape prior formulation. Our work builds on the contour flow framework proposed by Chen *et al.* (Chen et al., 2025), which introduces a mathematically derived constraint to preserve global shape similarity in image segmentation. By formulating this constraint from a contour flow perspective and integrating it into deep networks as a loss or via an unrolled variational model, their method improves segmentation accuracy and shape consistency across diverse datasets. We extend this foundation to explore elliptical shape-constrained segmentation. Existing methods (Slabaugh and Unal, 2005; Verma et al., 2014; Ukpai et al., 2014) commonly minimize the distance between the current segmentation result and a reference ellipse. In contrast, we guide the segmentation result to maintain the elliptical shape by constructing a contour field based on parameterized ellipses. Additionally, through the use of dual algorithms, we effectively integrate the elliptical prior with spatial regularization into the image segmentation model. Furthermore, we expand our variational model into a new network module, termed the ESP (Elliptical Shape Prior) module. We will demonstrate how this module can be seamlessly integrated into the Segment

Anything Model (SAM) (Kirillov et al., 2023). To the best of our knowledge, there is currently no literature on the SAM architecture ensuring that the shape of the image segmentation output is elliptical.

The main contributions of this paper are as follows:

- We propose an elliptical shape prior representation with the variational method by constraining the contour field.
- The proposed ellipse prior expression can be efficiently solved using a dual algorithm, allowing the incorporation of the ellipse prior into the design of deep network structures through a latent dual space.
- By decomposing SAM into mathematical sub-problems, we offer a new approach to integrate the elliptical shape prior into SAM.

The structure of this paper is outlined as follows: In Section 2, we introduce some related works. Section 3 presents the proposed model for image segmentation, which incorporates constraints for elliptical shapes. Following this, in Section 4, we introduce the ESP module and integrate it into SAM. We then demonstrate the performance of the proposed model through simple numerical experiments in Section 5. Section 6 presents the experimental results of the model on different datasets. Finally, in the concluding section, we provide a summary and discussion.

2 The Related Works

2.1 Potts Model

The Potts model (Potts, 1952) is a classical variational segmentation model that encompasses other variational segmentation models within its framework. The Potts model, after convexification and regularization improvements (Yuan et al., 2010), can be expressed as:

$$\mathbf{u}^* = \arg \min_{\mathbf{u} \in \mathbb{U}} \left\{ \sum_{i=1}^I \int_{\Omega} -o_i(\mathbf{x})u_i(\mathbf{x})d\mathbf{x} + \lambda \sum_{i=1}^I \int_{\Omega} |\nabla u_i(\mathbf{x})|d\mathbf{x} \right\}, \quad (1)$$

where Ω represents the image region, and I is the number of classes. $o_i(\mathbf{x})$ denotes the similarity of pixel \mathbf{x} to the i -th class. The second term in (1) is the Total Variation (TV) regularization, which quantifies the boundary length of the segmentation regions. The parameter λ modulates the trade-off between these terms, while the set

$$\mathbb{U} = \left\{ \mathbf{u} = (u_1, \dots, u_I) \in [0, 1]^I : \sum_{i=1}^I u_i(\mathbf{x}) = 1, \forall \mathbf{x} \in \Omega \right\}. \quad (2)$$

stands for the image segmentation condition.

Although the TV regularization term is widely used in image segmentation, its non-smoothness, sensitivity to the choice of the parameter λ , and boundary effects limit its effectiveness.

2.2 Threshold Dynamics Method for Regularization

A smooth and concave regularization term is proposed in papers (Esedoĝ Lu and Otto, 2015; Wang et al., 2017; Liu et al., 2022) as a replacement for the Total Variation (TV) term. This regularization term is defined as follows:

$$\sqrt{\frac{\pi}{\sigma}} \sum_{i=1}^I \int_{\Omega} u_i(\mathbf{x})(k * (1 - u_i))(\mathbf{x})d\mathbf{x}, \quad (3)$$

where “ $*$ ” denotes convolution and k is a kernel, like a 2-D Gaussian function $k(\mathbf{x}) = \frac{1}{2\pi\sigma^2} e^{-\frac{\|\mathbf{x}\|^2}{2\sigma^2}}$.

This regularization term accomplishes the task of segmenting image results into homogeneous regions by introducing penalties for the inconsistency between neighboring points and the segmentation class assigned to the central point. With this regularization, Liu *et al* (Liu et al., 2022) proposed the following Soft Threshold Dynamics (STD) regularized model:

$$\min_{\mathbf{u} \in \mathbb{U}} \{ \langle -\mathbf{o}, \mathbf{u} \rangle + \varepsilon \langle \mathbf{u}, \ln \mathbf{u} \rangle + \lambda \langle \mathbf{u}, k * (1 - \mathbf{u}) \rangle \}. \quad (4)$$

Here,

$$\lambda \langle \mathbf{u}, k * (1 - \mathbf{u}) \rangle = \lambda \sum_{i=1}^I \int_{\Omega} u_i(\mathbf{x})(k * (1 - u_i))(\mathbf{x})d\mathbf{x}. \quad (5)$$

referred to as $\mathcal{R}(\mathbf{u})$. Since this term is concave when k is symmetric and positive semi-definite, the objective function can be optimized using the difference of convex (DC) algorithm:

$$\mathbf{u}^{t+1} = \arg \min_{\mathbf{u} \in \mathbb{U}} \{ \langle -\mathbf{o} + \varepsilon \ln \mathbf{u}, \mathbf{u} \rangle + \mathcal{R}(\mathbf{u}^t) + \langle \mathbf{p}^t, \mathbf{u} - \mathbf{u}^t \rangle \}, \quad (6)$$

where $\mathbf{p}^t = \lambda k * (1 - 2\mathbf{u}^t) \in \partial \mathcal{R}(\mathbf{u}^t)$. This method exhibits high stability and rapid convergence in practical implementations, in contrast to TV regularization (Liu et al., 2022). Therefore, we will adopt this regularization term instead of the TV term in our model.

2.3 Active Contour with Elliptical Shape Prior

Active contour models, introduced by Kass *et al.* (Kass et al., 1987), combine image data and geometric properties into an energy function. Minimizing this function allows the contour to converge to the target edge from its initial position. The general energy function consists of internal and external energy components:

$$E(\mathbf{v}) = \int_0^1 E_{int}(\mathbf{v}(s)) + E_{ext}(\mathbf{v}(s)) ds. \quad (7)$$

Here, $\mathbf{v}(s) = (x(s), y(s))$, $s \in [0, 1]$ represents the contour curve. The internal energy E_{int} ensures curve continuity and smoothness, while the external energy E_{ext} is generally defined by the image gradient.

To attain particular contour shapes, an additional shape energy term E_{shape} is frequently integrated into (7). When imposing circular constraints, this term quantifies the deviation from a reference circle (Wu et al., 2013).

$$E_{shape} = \int_0^1 (|\mathbf{v}(s) - \mathbf{v}_0| - R)^2 ds, \quad (8)$$

where \mathbf{v}_0 and R indicate the center and radius of the reference circle, respectively.

For elliptical shape constraints, Verma *et al.* (Verma et al., 2014) used a polar coordinate representation, $\mathbf{v}(\theta) = \rho(\theta)e^{j\theta}$, $\theta \in [0, 2\pi]$ represents the contour curve, and the reference ellipse $\mathbf{v}_e = \rho_e(\theta)e^{j\theta}$. They defined the E_{shape} as follows:

$$E_{shape} = \int_0^{2\pi} (\rho(\theta) - \rho_e(\theta))^2 d\theta. \quad (9)$$

To achieve a more precise fit, Ukpai *et al.* (Ukpai et al., 2014) introduced scaling, rotation, and translation transformations into the energy term.

The active contour method is widely acknowledged as an effective approach. The integration of elliptical shape priors within the active contour method has shown promise in enhancing segmentation accuracy for specific tasks (Verma et al., 2014; Ukpai et al., 2014; Wu et al., 2013). However, this method's success heavily hinges upon the initial contour selection and is susceptible to convergence to local minima.

2.4 Segment Anything Model

SAM (Kirillov et al., 2023) is a novel general-purpose visual segmentation model, which consists of three key components: an image encoder, a prompt encoder, and a mask decoder. Specifically, the image encoder, based on the Vision Transformer (ViT) (Dosovitskiy et al., 2021), maps images to a high-dimensional embedding space, denoted as $\mathcal{T}_{\theta_1}^1$. The prompt encoder converts positional prompts to 256-dimensional embeddings, denoted as $\mathcal{T}_{\theta_2}^2$. The mask decoder employs two transformer modules to merge image embeddings with prompt features and uses transposed convolution layers for upsampling, followed by MLP layers to map the output tokens to a dynamic classifier.

To combine with the elliptical shape prior proposed in this paper later, we first express SAM as mathematical sub-problems. Let $I \in \mathbb{R}^{h \times w}$ denotes the input image and $P \in \mathbb{R}^k$ represents the input prompt with k tokens. The parameterized encoding operators $\mathcal{T}_{\theta_1}^1 : \mathbb{R}^{h \times w} \rightarrow \mathbb{R}^{h_1 \times w_1 \times c_1}$ and $\mathcal{T}_{\theta_2}^2 : \mathbb{R}^k \rightarrow \mathbb{R}^{k \times c_1}$ respectively map the image and prompt to features. To integrate features from these two different spaces, a fusion operator $\mathcal{T}_{\theta_3}^3 : \mathbb{R}^{h_1 \times w_1 \times c_1} \times \mathbb{R}^{k \times c_1} \rightarrow \mathbb{R}^{h \times w}$ would be introduced. Operator $\mathcal{T}_{\theta_3}^3$ includes cross-attention, MLP and upscale operation. Then we can write the SAM as:

$$\begin{cases} \tilde{I} = \mathcal{T}_{\theta_1}^1(I), \tilde{P} = \mathcal{T}_{\theta_2}^2(P), \\ o = \mathcal{T}_{\theta_3}^3(\tilde{I}, \tilde{P}), \\ u = \mathcal{F}(o). \end{cases} \quad (10)$$

Here o is the extracted feature by SAM, and \mathcal{F} is a decoding operator. In the simplest case, \mathcal{F} can be the Heaviside step function defined as follows:

$$\mathcal{F}(o)(x) = \begin{cases} 0, & o(x) \leq 0, \\ 1, & o(x) > 0. \end{cases} \quad (11)$$

The backward propagation derivative of this non-differentiable function at 0 is usually handled with special treatment by automatic differentiation in PyTorch and TensorFlow.

The final output of SAM is given by $u \in [0, 1]^{h \times w}$. In summary, we represent SAM as the above four sub-problems: where $\mathcal{T}_{\theta_1}^1$, $\mathcal{T}_{\theta_2}^2$ are encoding processes, $\mathcal{T}_{\theta_3}^3$ primarily involves the cross attention feature fusion step, and \mathcal{F} is the decoding process.

To apply SAM to downstream tasks, Chen *et al.* (Chen et al., 2023) introduced SAM-adapter, which consists of only two MLP layers inserted between the transformer layers of the image encoder. This integration enables the model to learn task-specific information.

For adapting SAM to retinal image segmentation, Qiu *et al.* proposed a modification (Qiu et al., 2023) where they fixed the parameters of the image encoder and introduced a learnable prompt layer between each transformer layer. This prompt layer incorporates convolutional layers, layer normalization, and GELU activation. Additionally, they replaced the original prompt encoder and mask decoder with a trainable task head composed of convolutional and linear layers.

Similarly, Zhang *et al.* (Zhang et al., 2024) devised an Adapter-Scale comprising Downscale, ReLU, and Upscale layers after the partial multi-head self-attention blocks in SAM’s image encoder. Additionally, they added an Adapter-Feature, constituted by two MLP layers, between transformer layers to merge high-frequency image information. These methods all involve augmenting SAM’s image encoder with learnable network layers, termed adapters. However, the rationale behind selecting these adapters lacks explicit mathematical justification.

In (Zhang et al., 2023), Zhang *et al.* emphasized the inclination of SAM segmentation results towards texture rather than shape. In this paper, we primarily focus on the decoding process, aiming to integrate the ellipse prior into this process. It is worth noting that when \mathcal{F} is the Heaviside step function, it can be equivalent to the minimization problem

$$\mathcal{F}(o) = \arg \min_{u \in [0,1]} \{-o, u\}. \quad (12)$$

This equivalent optimization problem will be utilized in our subsequent method.

3 The Proposed Method

The objective of image segmentation is to obtain a segmentation function u that is consistent with the ground truth. In this section, we use elliptical contour field to mathematically impose elliptical shape constraint on the segmentation function u and incorporate this constraint into the image segmentation model.

3.1 Elliptical Shape Prior based on Contour Flow

The geometric characteristics of an ellipse are defined by its center point (x_0, y_0) , major and minor axes a, b , and a rotation angle θ about the center. An ellipse with parameter $\Lambda := (x_0, y_0, a, b, \theta)$ can be represented as follows:

$$\frac{((x - x_0) \cos \theta + (y - y_0) \sin \theta)^2}{a^2} + \frac{(-(x - x_0) \sin \theta + (y - y_0) \cos \theta)^2}{b^2} = 1.$$

For the convenience of subsequent expressions, let us represent the above ellipse equation in parametric form

$$\begin{cases} x = \phi(t) := a \cos \theta \cos t - b \sin \theta \sin t + x_0, \\ y = \psi(t) := a \sin \theta \cos t + b \cos \theta \sin t + y_0, \end{cases} \quad (13)$$

where $t \in (0, 2\pi]$. Then the tangent vector of the ellipse can be written as $\mathbf{T}_\Lambda(x, y) = (\phi'(t), \psi'(t))$.

In the Cartesian coordinate system, \mathbf{T}_Λ is formulated as:

$$\begin{aligned} \mathbf{T}_\Lambda(x, y) = & ((x - x_0)(b^2 - a^2) \cos \theta \sin \theta + (y - y_0)(b^2 \sin^2 \theta + a^2 \cos^2 \theta), \\ & (y - y_0)(a^2 - b^2) \cos \theta \sin \theta - (x - x_0)(a^2 \sin^2 \theta + b^2 \cos^2 \theta)). \end{aligned} \quad (14)$$

To ensure that the segmentation results exhibit elliptical shapes, we do not impose direct constraints on $u(x, y)$. Inspired by Chen *et al.* (Chen et al., 2025), we enforce an orthogonality constraint between its gradient $\nabla u(x, y)$ and a tangent vector field $\mathbf{T}_\Lambda(x, y)$ determined by a given parameter Λ . In fact, it can be proven that if $\langle \nabla u(x, y), \mathbf{T}_\Lambda(x, y) \rangle = 0, \forall (x, y) \in \Omega$, then the contours of u must be ellipses, as stated in the following proposition.

Proposition 1. *Suppose both $u : \Omega \subset \mathbb{R}^2 \rightarrow [0, 1]$ and its contours be \mathcal{C}^1 , and $\mathbf{T}_\Lambda(x, y)$ is the tangent vector field determined by (14). Then we have all the contours of $u(x, y)$ are concentric ellipses with the same orientation if and only if $\exists \Lambda$, s.t. $\langle \nabla u(x, y), \mathbf{T}_\Lambda(x, y) \rangle = 0, \forall (x, y) \in \Omega$.*

Please find the proof in the Appendix A. For notational simplicity, we directly denote \mathbf{T}_Λ as \mathbf{T} below. Now, let us define

$$\mathbb{P} = \{u : \langle \nabla u(x, y), \mathbf{T}(x, y) \rangle = 0, \forall (x, y) \in \Omega\}.$$

According to the Proposition 1, if $u \in \mathbb{P}$, then all the contours of u must be ellipses. Please note that \mathbb{P} is a convex set, making it easy to satisfy the constraint $u \in \mathbb{P}$ using the dual method in the variational problem. Therefore, we can propose an image segmentation model with our elliptical shape prior as follows.

3.2 Our Model with Elliptical Shape Prior

Our model can be given as:

$$\min_{\mathbf{u} \in \mathbb{U}, u_i \in \mathbb{P}, \mathbf{T}} \{ \langle -\mathbf{o}, \mathbf{u} \rangle + \varepsilon \langle \mathbf{u}, \ln(\mathbf{u}) \rangle + \mathcal{R}(\mathbf{u}) \}, \quad (15)$$

where u_i is the segmentation function of i -th region which has to be elliptical shape, $\mathcal{R}(\mathbf{u})$ denotes the threshold dynamic regularization term (Liu et al., 2022) mentioned earlier in (5).

The above model differs from the existing model (4) in three main aspects: Firstly, by imposing $u_i \in \mathbb{P}$, we constrain the segmentation regions of the i -th class of interest to satisfy the elliptical shape prior. Secondly, in order to satisfy the smoothness condition of u_i mentioned in Proposition 1, we add the second term as an entropy regularization term, in which the parameter $\varepsilon > 0$ controls the smoothness of u_i . If $\varepsilon \rightarrow 0^+$, then the segmentation function \mathbf{u} tends to be binary. Thirdly, we need to estimate the tangent vector field of the prior ellipses, which enables the model to find the optimal elliptical segmentation region.

According to the Lagrange multiplier method, we can obtain the following equivalent dual problem:

$$\min_{\mathbf{u} \in \mathbb{U}, \mathbf{T}} \max_q \{ \langle -\mathbf{o}, \mathbf{u} \rangle + \mathcal{R}(\mathbf{u}) + \varepsilon \langle \mathbf{u}, \ln(\mathbf{u}) \rangle - \langle q, \mathbf{T} \cdot \nabla u_i \rangle \}, \quad (16)$$

where the variable $q(x, y)$ represents the dual variable (Lagrange multiplier). By using the conjugate formula, we obtain: $\langle q, \mathbf{T} \cdot \nabla u_i \rangle = -\langle \text{div}(q\mathbf{T}), u_i \rangle$ with the Neumann boundary condition $\frac{\partial u_i}{\partial \mathbf{n}} = 0$. Here ‘‘div’’ is the divergence operator which is the conjugate operator of the gradient. Thus, we can rewrite (16) as:

$$\min_{\mathbf{u} \in \mathbb{U}, \mathbf{T}} \max_q \left\{ \underbrace{\langle -\mathbf{o}, \mathbf{u} \rangle + \mathcal{R}(\mathbf{u}) + \varepsilon \langle \mathbf{u}, \ln(\mathbf{u}) \rangle + \langle \text{div}(q\mathbf{T}), u_i \rangle}_{\mathcal{E}(\mathbf{u}, q, \mathbf{T})} \right\}. \quad (17)$$

By applying the alternating algorithm, we obtain the following three subproblems:

$$\begin{cases} q^{t+1} = \arg \max_q \mathcal{E}(\mathbf{u}^t, q, \mathbf{T}^t), \\ \mathbf{u}^{t+1} = \arg \min_{\mathbf{u} \in \mathbb{U}} \mathcal{E}(\mathbf{u}, q^{t+1}, \mathbf{T}^t), \\ \mathbf{T}^{t+1} = \arg \min_{\mathbf{T}} \mathcal{E}(\mathbf{u}^{t+1}, q^{t+1}, \mathbf{T}). \end{cases} \quad (18)$$

The first subproblem associated with variable q can be effectively solved using the gradient ascent algorithm

$$q^{t+1} = q^t - \tau_q \mathbf{T}^t \cdot \nabla u_i^t, \quad (19)$$

where $\tau_q > 0$ is a step parameter.

For the second subproblem related to \mathbf{u} , we can employ the DC (Difference of Convex functions) algorithm. By replacing $\mathcal{R}(\mathbf{u})$ with its supporting hyperplane (Liu et al., 2022), one can get:

$$\mathbf{u}^{t+1} = \arg \min_{\mathbf{u} \in \mathbb{U}} \{ \langle -\mathbf{o} + \mathbf{p}^t, \mathbf{u} \rangle + \varepsilon \langle \mathbf{u}, \ln(\mathbf{u}) \rangle + \langle \text{div}(q^{t+1}\mathbf{T}^t), u_i \rangle \}.$$

Here $\mathbf{p}^t = \lambda k * (1 - 2\mathbf{u}^t) \in \partial \mathcal{R}(\mathbf{u}^t)$ is a subgradient of $\mathcal{R}(\mathbf{u})$ as shown in (6). This \mathbf{u} -subproblem is a strictly convex optimization problem, guaranteeing the existence of a unique solution. Furthermore, this solution takes the form of a closed-form softmax expression:

$$u_i^{t+1} = \frac{e^{\frac{\sigma_i - p_i^t - \delta_{i,i} \text{div}(q^{t+1}\mathbf{T}^t)}{\varepsilon}}}{\sum_{i'}^I e^{\frac{\sigma_{i'} - p_{i'}^t - \delta_{i',i'} \text{div}(q^{t+1}\mathbf{T}^t)}{\varepsilon}}}, \quad \hat{i} = 1, \dots, I. \quad (20)$$

Algorithm 1 Image segmentation with elliptical shape prior

Input: The image feature \mathbf{o} .

Output: Segmentation function \mathbf{u} , where u_i represents the indicator function for the ellipse region.

Initialization: $u_i^0 = [\text{softmax}(\mathbf{o})]_i = \frac{e^{\frac{o_i}{\sigma_i}}}{\sum_{i'} e^{\frac{o_{i'}}{\sigma_{i'}}}}$, dual variable $q^0 = 0$, and a tangent vector field \mathbf{T}^0 .

for $t = 0, 1, 2, \dots$ **do**

 1. Solve the first subproblem using the gradient ascent algorithm to update variable q^{t+1} according to (19):

$$q^{t+1} = q^t - \tau_q \mathbf{T}^t \cdot \nabla u_i^t.$$

 2. Solve the second subproblem using the DC algorithm to update variable \mathbf{u}^{t+1} according to (20):

$$\mathbf{u}_i^{t+1} = \text{softmax}(\mathbf{o}_i - \mathbf{p}_i^t - \delta_{\hat{i}, i} \text{div}(q^{t+1} \mathbf{T}^t)).$$

 3. Obtain the parameter values for \mathbf{T}^{t+1} based on (22) and update \mathbf{T}^{t+1} according to (14).

4. Convergence check. If it is converged, end the algorithm.

end for

Here $\delta_{\hat{i}, i}$ is the Delta function defined by $\delta_{\hat{i}, i} = 0$ when $\hat{i} \neq i$ and $\delta_{\hat{i}, i} = 1$. More details for calculating u^{t+1} can be found in Appendix B.

Now let us solve the third subproblem. First, we note that \mathbf{T} is determined by parameter $\Lambda = (x_0, y_0, a, b, \theta)$. Directly solving this subproblem to update the parameter Λ entails a substantial computational burden. In (Leung et al., 2004), the authors utilized the second-order moment of the membership function to obtain the relevant parameters of the best-fitting ellipse. We follow the same approach. In fact, if u_i denote the indicator function representing an elliptical region. Then we have the following formulas:

$$\begin{cases} \iint_{\Omega} u_i(x, y) dx dy = \pi ab, \\ \iint_{\Omega} x u_i(x, y) dx dy = x_0 \pi ab, \\ \iint_{\Omega} y u_i(x, y) dx dy = y_0 \pi ab, \\ \iint_{\Omega} (x - x_0)^2 u_i(x, y) dx dy = \frac{(a^2 \cos^2 \theta + b^2 \sin^2 \theta)}{C}, \\ \iint_{\Omega} (y - y_0)^2 u_i(x, y) dx dy = \frac{(a^2 \sin^2 \theta + b^2 \cos^2 \theta)}{C}, \\ \iint_{\Omega} (y - y_0)(x - x_0) u_i(x, y) dx dy = \frac{(a^2 - b^2) \cos \theta \sin \theta}{C}. \end{cases} \quad (21)$$

where $C = \frac{4}{ab\pi}$. Since we only need to update \mathbf{T} , based on equation (21), we obtain the following scheme to update the important quantities related to \mathbf{T}^{t+1} :

$$\begin{cases} x_0^{t+1} = \frac{\sum_{x,y} x u_i^{t+1}(x,y)}{\sum_{x,y} u_i^{t+1}(x,y)}, y_0^{t+1} = \frac{\sum_{x,y} y u_i^{t+1}(x,y)}{\sum_{x,y} u_i^{t+1}(x,y)}, \\ ((a^{t+1})^2 - (b^{t+1})^2) \cos \theta^{t+1} \sin \theta^{t+1} = \frac{4M_{xy}}{\sum_{x,y} u_i^{t+1}(x,y)}, \\ (b^{t+1})^2 \sin^2 \theta^{t+1} + (a^{t+1})^2 \cos^2 \theta^{t+1} = \frac{4M_{xx}}{\sum_{x,y} u_i^{t+1}(x,y)}, \\ (a^{t+1})^2 \sin^2 \theta^{t+1} + (b^{t+1})^2 \cos^2 \theta^{t+1} = \frac{4M_{yy}}{\sum_{x,y} u_i^{t+1}(x,y)}. \end{cases} \quad (22)$$

where $M_{xx} = \sum_{x,y} (x - x_0^{t+1})^2 u_i^{t+1}(x, y)$, $M_{yy} = \sum_{x,y} (y - y_0^{t+1})^2 u_i^{t+1}(x, y)$, $M_{xy} = \sum_{x,y} (x - x_0^{t+1})(y - y_0^{t+1}) u_i^{t+1}(x, y)$

represent the second moments. Once we obtain the values for the parameters mentioned above, we can update \mathbf{T}^{t+1} according to equation (14). In summary, Algorithm 1 outlines the steps to solve the proposed model.

4 Integrated into the Segment Anything Model

In this section, we will unroll the alternating iterative process of Algorithm 1 into a neural network architecture, then integrate it into the SAM.

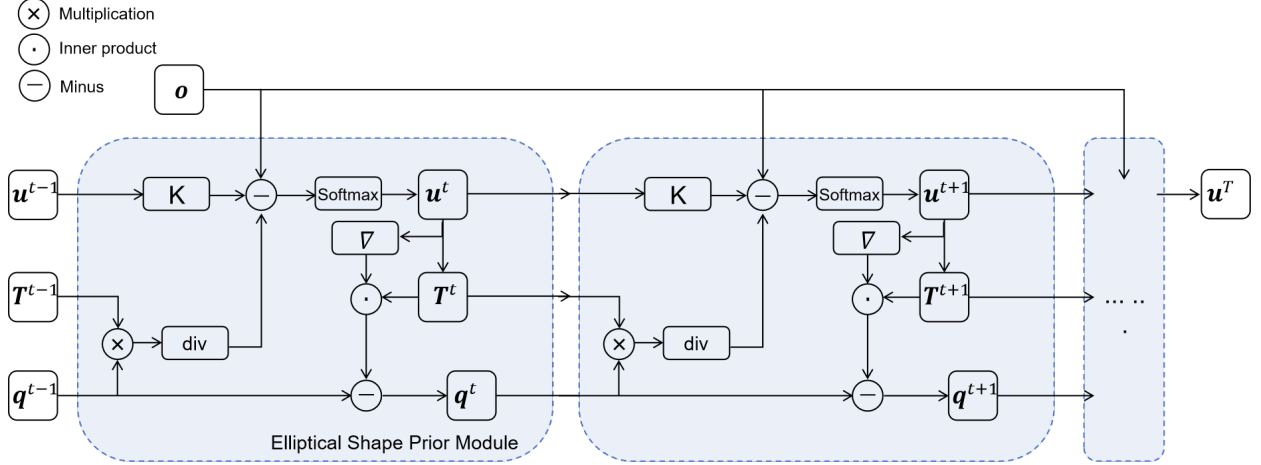


Figure 1: Architecture of each elliptical shape prior (ESP) module.

4.1 Elliptical Shape Prior (ESP) Module

It can be observed that the final layer equation (12) of the SAM model corresponds to a hard K-means clustering problem. Therefore, the optimization problem (12) can be approximated using the following smoothed version

$$u_\varepsilon = \arg \min_{u \in [0,1]} \{ \langle -o, u \rangle + \varepsilon (\langle u, \ln u \rangle + \langle 1 - u, \ln (1 - u) \rangle) \}. \quad (23)$$

We incorporate our elliptical constraint into equation (23) and replace the final subproblem of the SAM (10) with this variational problem, yielding

$$\begin{cases} \tilde{I} = \mathcal{T}_{\theta_1}^1(I), \tilde{P} = \mathcal{T}_{\theta_2}^2(P), \\ o = \mathcal{T}_{\theta_3}^3(\tilde{I}, \tilde{P}), \\ u, \mathbf{T} = \arg \min_{u \in [0,1] \cap \mathbb{P}, \mathbf{T}} \{ \langle -o, u \rangle + \mathcal{R}(u) + \varepsilon (\langle u, \ln u \rangle + \langle 1 - u, \ln (1 - u) \rangle) \}. \end{cases} \quad (24)$$

The third sub-equation in (24) represents the scenario of our model (15) in binary segmentation. This ensures that the decoder of SAM produces smooth elliptical object.

We unroll the Algorithm 1 for solving the modified variational problem into several network layers. Specifically, the operators ∇ and “div” in the alternating iterative scheme are replaced with fixed kernel convolution layers representing discrete gradient and divergence, respectively. According to Algorithm 1, each ESP module outputs an intermediate segmentation function u^t , which is used to compute u^{t+1} for the subsequent module. The specific structure of the ESP module is illustrated in Figure 1. For simplification, we call SAM with this decoding module as SAM-ESP.

5 The Performance of ESP Module

In this section, we design two very simple experiments to show the intuition of the proposed Algorithm 1.

5.1 Synthetic Image Experiment

Initially, our model is tested on a non-elliptical synthetic image. For this experiment, we choose the region variance as the similarity $o_i(x) = -\|h(x) - m_i\|^2$ for $i = 1, 2$. Here m_1 and m_2 represent the average gray value of the foreground and background, respectively. The parameter λ for \mathcal{R} and the entropy regularization parameter ε are set to 1. A higher λ value is beneficial for boundary smoothing, whereas a smaller ε value is preferable for binary segmentation. We utilize a Gaussian kernel function with a support set size of 5×5 and a standard deviation of 5, denoted as kernel k . We set $\tau_q = 1$ for our test. As shown in Figure 2, after 500 iterations, our model successfully transformed the non-elliptical region into an ellipse.

Throughout the iteration process, our model ensures orthogonality between the normal vector field of the image segmentation results and the tangent vector field of the ellipses. This alignment facilitates the transformation of the regions into elliptical shapes.

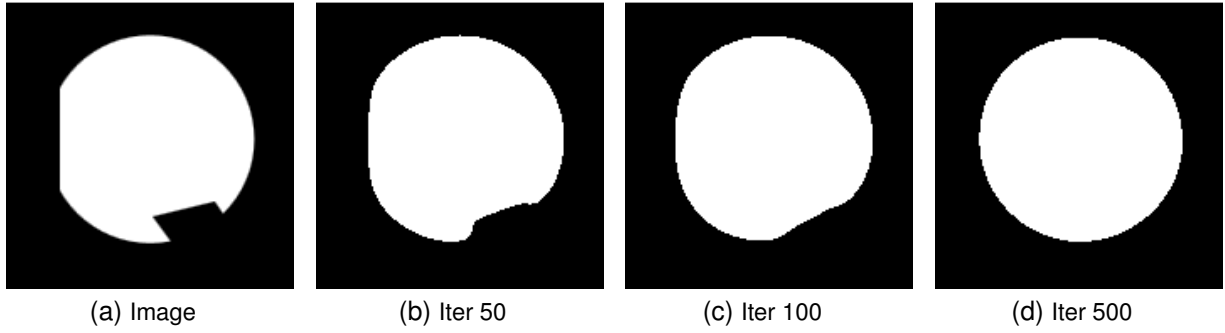


Figure 2: The proposed method for a non-elliptical region.

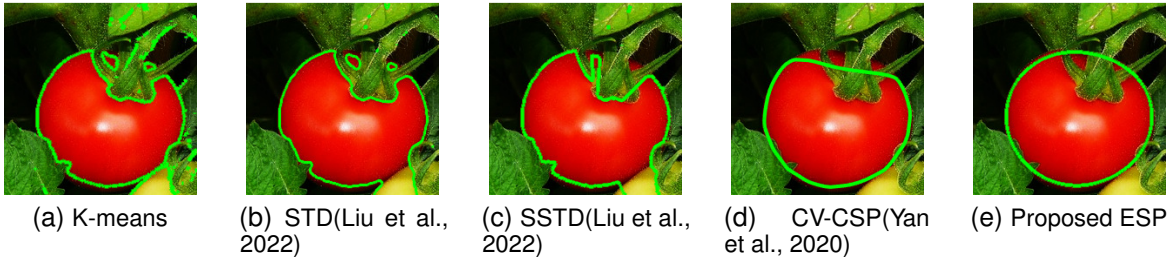


Figure 3: The comparison of different methods on a natural image.

5.2 Natural Image Segmentation

The second experiment evaluates the algorithm’s performance on natural images. We select an image of a tomato and compare the result with segmentation models that incorporate different shape priors: star-shaped prior (SSTD) (Liu et al., 2022) and convexity prior (CV-CSP) (Yan et al., 2020).

In this numerical experiment, the similarity $o_i(x) = -(\mathbf{h}(x) - \mathbf{m}_i)^\top \Sigma_i^{-1} (\mathbf{h}(x) - \mathbf{m}_i)$, for $i = 1, 2$. Here \mathbf{m}_i and Σ_i are the mean and covariance matrix of object and background, respectively. The convergence standard is $\|\mathbf{u}^t - \mathbf{u}^{t+1}\| < 3 \times 10^{-5}$. For SSTD (Liu et al., 2022), we replace the center of the star-shaped regions with their centroids.

The comparison results are shown in Figure 3. Compared to K-means, both STD (Liu et al., 2022), SSTD (Liu et al., 2022), and CV-CSP (Yan et al., 2020) methods provide smooth segmentation boundaries due to the presence of regularization terms. However, due to occlusion by green leaf stems, they fail to extract the entire tomato. In contrast, our algorithm effectively segments the tomato. This straightforward numerical illustration highlights the effectiveness of the proposed algorithm in segmenting elliptical regions.

6 Numerical Experimental Results of SAM-ESP

In this section, we will train SAM-ESP on several datasets and compare the experimental results with the original SAM, fine-tuned SAM, and two other methods of incorporating priors into neural network architectures, namely post-processing and loss function modification. The experimental results demonstrate that SAM-ESP achieves the best segmentation outcomes and exhibits greater stability.

6.1 Training Protocol and Experimental Setup

SAM offers three different scales of image encoders: ViT-B, ViT-L, and ViT-H. ViT-L and ViT-H only have slight improvements over ViT-B but require significantly more computation (Kirillov et al., 2023). Therefore, we choose ViT-B as the image encoder.

We maintain the core architecture of SAM. During training, all trainable parameters within the image encoder and mask decoder are updated while the prompt encoder is frozen as it proficiently encodes bounding box prompts. The detailed

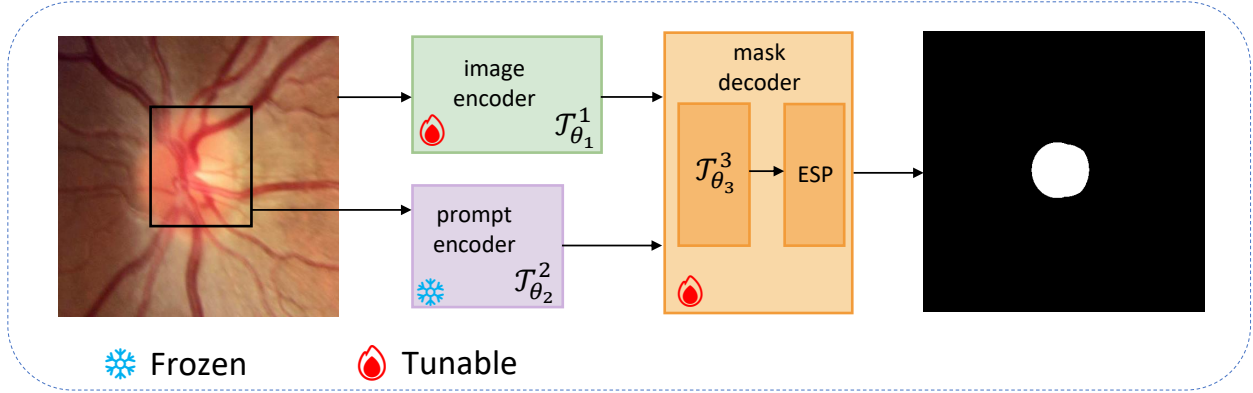


Figure 4: The network architecture of SAM-ESP.

architecture of the entire network is illustrated in Figure 4. Throughout the training process, each image is provided with bounding box prompts derived from the minimum bounding box containing the ground truth, with random perturbations ranging from 0 to 40 pixels. The entropy parameter ε , regularization parameter λ , and gradient update rate τ_q in the ESP module are all set to 1. A total of 100 ESP modules are deployed. The loss function employed during training is the cross-entropy loss \mathcal{L}_{CE} . We utilize the Adam optimizer with default parameters. The training is implemented on an NVIDIA Tesla V100 GPU and the batch size for all data is set to 1. After the training is finished, the model with the best performance on the validation set is selected for testing. For comparison, we fine-tuned SAM using the same training strategy, which we refer to as SAM-fine.

To better compare the incorporation of the elliptical prior into the SAM model in different ways, we attempt another two different ways. The first method is the post-processing method. We use the output feature \mathbf{o} of SAM-fine as the input for Algorithm 1, iterating the algorithm 100 times to obtain the elliptical shape. We denote this as SAM-post. In this approach, the elliptical prior cannot guide the learning of the main network through backpropagation.

The second method of incorporating priors into the network, namely the loss function method. We can design a shape loss \mathcal{L}_S based on cosine distance, as provided by Proposition 1, to impose shape constraints:

$$\mathcal{L}_S := \sum_{x \in \Omega} \frac{|\nabla \mathbf{u}(x) \cdot \mathbf{T}(x)|}{\|\nabla \mathbf{u}(x)\|}. \quad (25)$$

Here, \mathbf{T} should represent the tangent vector field of the ellipse. Considering that the ground truth in the selected dataset are ellipses, we employ the contour flow field (Chen et al., 2025) of the ground truth as \mathbf{T} . By adding this shape loss term to the cross-entropy loss, the final loss function is defined as:

$$\mathcal{L} = \lambda_l \mathcal{L}_{CE} + (1 - \lambda_l) \mathcal{L}_S.$$

We utilize this loss to train SAM, with the parameter λ_l set to 0.4 during training. The model trained with this loss function is denoted as SAM-Sloss. In this method, the elliptical prior has limited influence during the prediction process, and small input perturbations in the network can render the elliptical prior ineffective.

6.2 Datasets

The proposed method is primarily validated and evaluated on datasets consisting of elliptical-shaped objects. The datasets selected ranges from 98 to 1200 images, each with varying resolutions. Figure 5 illustrates sample images from the datasets, while Table 1 presents the data preprocessing details for the datasets used.

- Retinal Fundus Glaucoma Dataset(Orlando et al., 2020): The Retinal Fundus Glaucoma Challenge (REFUGE) was organized by MICCAI in 2018. Following the procedure outlined by Liu(Liu et al., 2022), we extract a 512×512 region of interest (ROI) for segmentation. The boundary of the optic cup is typically more blurred compared to the optic disc, making accurate segmentation of the optic cup region challenging. Considering that the optic cup is predominantly elliptical in shape, we train our model specifically for cup segmentation on this dataset and the learning rate is set to 1e-4 with 100 epochs.
- Automatic Cardiac Diagnosis Challenge Dataset(Bernard et al., 2018): The Automatic Cardiac Diagnosis Challenge (ACDC) dataset was initiated by MICCAI in 2017. This dataset includes MRI scans from 100

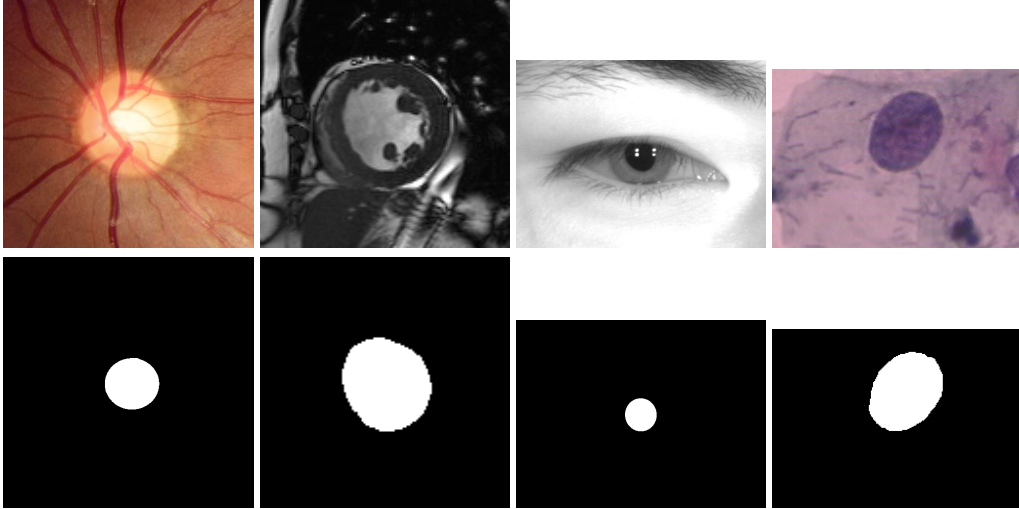


Figure 5: Sample images from the datasets used. From left to right, columns one to four are from REFUGE, ACDC, CASIA.v4-distance, DTU/Herlev dataset respectively. The first row shows the images, whose ground truth segmentations displayed at the second row.

Table 1: Data preprocessing of the datasets used.

Dataset	Image size	Image quantity	Train-Validate-Test
REFUGE	512×512	1200	400-400-400
ACDC	128×128	450	100-100-250
CASIA.v4	640×480	395	100-196-99
DTU/Herlev	*	98	20-20-58

patients with expert segmentations. Given the typically elliptical shape of the left ventricle, we focused on training and evaluating segmentation performance on this structure. We select data from 10 patients for training, 10 for validation, and 25 for testing, with each patient providing 10 images. On this dataset, the learning rate is set to $5e-5$ with 50 epochs.

- CASIA.v4-distance(Test): CASIA.v4-distance is a subset of the CASIA.v4 database collected by the Chinese Academy of Sciences’ Institute of Automation. In this study, we utilize a subset provided in (Wang et al., 2020) to train the model for pupil segmentation. The pupil masks were manually annotated by the authors of (Wang et al., 2020). We employ 100 of these images for training, utilize 196 images for validation, and reserve the remaining 99 images for testing. On this dataset, the learning rate is set to $1e-4$ with 50 epochs.
- DTU/Herlev Dataset(Jantzen et al., 2005): The DTU/Herlev dataset consists of 917 single-cell Papanicolaou-stained images. Given that cell nuclei generally exhibit an elliptical shape, we extract 98 images from this dataset to validate our model. Specifically, 20 images are allocated for training, another 20 for validating, and the remaining 58 for testing. Our model underwent training for 50 epochs with a learning rate set at $5e-5$.

6.3 Evaluation Metrics

6.3.1 Dice Similarity Coefficient (Dice)

The Dice similarity coefficient between the predicted mask P and the ground truth G is defined as:

$$\text{Dice} = \frac{2|P \cap G|}{|P| + |G|} \quad (26)$$

Dice quantifies the overlap between the predicted and ground truth segmentations within the range $0 \leq \text{Dice} \leq 1$, with 1 indicating perfect alignment between the segmentations.

Table 2: Computational Efficiency Comparison (Trn T: Training Time per epoch; Inf T: Inference Time per image).

Method	REFUGE		ACDC	
	Trn T	Inf T	Trn T	Inf T
SAM-fine	1.79min	80.23ms	0.34min	80.50ms
SAM-Sloss	2.91min	80.02ms	0.38min	80.83ms
SAM-ESP	4.28min	178.80ms	1.01min	150.16ms
Method	CASIA.v4		DTU/Herlev	
	Trn T	Inf T	Trn T	Inf T
SAM-fine	0.36min	80.74ms	0.10min	71.73ms
SAM-Sloss	1.05min	81.08ms	0.11min	72.35ms
SAM-ESP	1.21min	166.90ms	0.44min	149.50ms

Table 3: Test Results on Four Datasets.

Dataset	Network	Dice \uparrow	BD \downarrow	BDS \downarrow	Dataset	Network	Dice \uparrow	BD \downarrow	BDS \downarrow
REFUGE	SAM	60.74	18.44	11.17	ACDC	SAM	49.03	13.32	8.12
	SAM-fine	87.62 \pm 0.30	7.38 \pm 0.27	4.35 \pm 0.11		SAM-fine	95.41 \pm 0.38	0.88 \pm 0.08	0.88 \pm 0.08
	SAM-post	87.76 \pm 0.32	7.28 \pm 0.28	4.23 \pm 0.14		SAM-post	95.50 \pm 0.39	0.83 \pm 0.06	0.81 \pm 0.05
	SAM-Sloss	88.78 \pm 0.15	6.67 \pm 0.08	3.87 \pm 0.07		SAM-Sloss	95.51 \pm 0.20	0.86 \pm 0.03	0.90 \pm 0.03
	SAM-ESP	89.07 \pm 0.14	6.36 \pm 0.11	3.75 \pm 0.13		SAM-ESP	95.85 \pm 0.09	0.76 \pm 0.004	0.78 \pm 0.01
CASIA.v4	SAM	67.29	13.85	10.85	DTU/ Herlev	SAM	48.69	11.07	7.72
	SAM-fine	95.37 \pm 0.41	1.80 \pm 0.10	1.23 \pm 0.12		SAM-fine	95.54 \pm 0.37	1.77 \pm 0.17	1.77 \pm 0.20
	SAM-post	95.51 \pm 0.41	1.74 \pm 0.10	1.17 \pm 0.10		SAM-post	95.80 \pm 0.32	1.43 \pm 0.12	1.28 \pm 0.14
	SAM-Sloss	94.12 \pm 0.14	2.60 \pm 0.05	1.79 \pm 0.06		SAM-Sloss	95.92 \pm 0.26	1.47 \pm 0.03	1.31 \pm 0.03
	SAM-ESP	95.62 \pm 0.18	1.74 \pm 0.04	1.22 \pm 0.02		SAM-ESP	96.45 \pm 0.16	1.36 \pm 0.10	1.47 \pm 0.18

*SAM denotes the Segment Anything Model without fine-tuning, SAM-fine indicates the fine-tuned Segment Anything Model, and SAM-post refers to the post-processed results of the SAM-fine. SAM-Sloss refers to the model trained with the shape loss.

6.3.2 Boundary Distance (BD)

Boundary Distance assesses the accuracy of object boundaries in segmentation results. Let e_G and e_P represent the edge pixels of the ground truth and predicted segmentations, respectively. BD is calculated as:

$$BD = \sum_{x_i \in e_P} \frac{D(x_i, e_G)}{|e_P|} \quad (27)$$

where $D(x_i, e_G) = \min_{x_j \in e_G} \|x_i - x_j\|$, representing the Euclidean distance between pixel x_i on the predicted boundary and its nearest pixel on the ground truth boundary.

6.3.3 Boundary Distance Standard Deviation (BDS)

The Boundary Distance Standard Deviation serves as an effective measure to assess the similarity in shape between predicted masks and ground truth values, which is defined as:

$$BDS = \sqrt{\frac{\sum_{x_i \in e_P} (D(x_i, e_G) - BD)^2}{|e_P|}} \quad (28)$$

A smaller BDS value reflects minimal fluctuations in distance between pixels along the segmentation boundary and the corresponding boundary in the ground truth, implying a higher level of shape similarity between the two.

6.4 Training and Inference Time

During the training process, our proposed shape loss \mathcal{L}_S and ESP module introduces some additional computational overhead. We present the detailed training and inference times of different methods in Table 2.

6.5 Performances and Analyses

Table 3 presents the segmentation performance results on the test sets of various datasets.

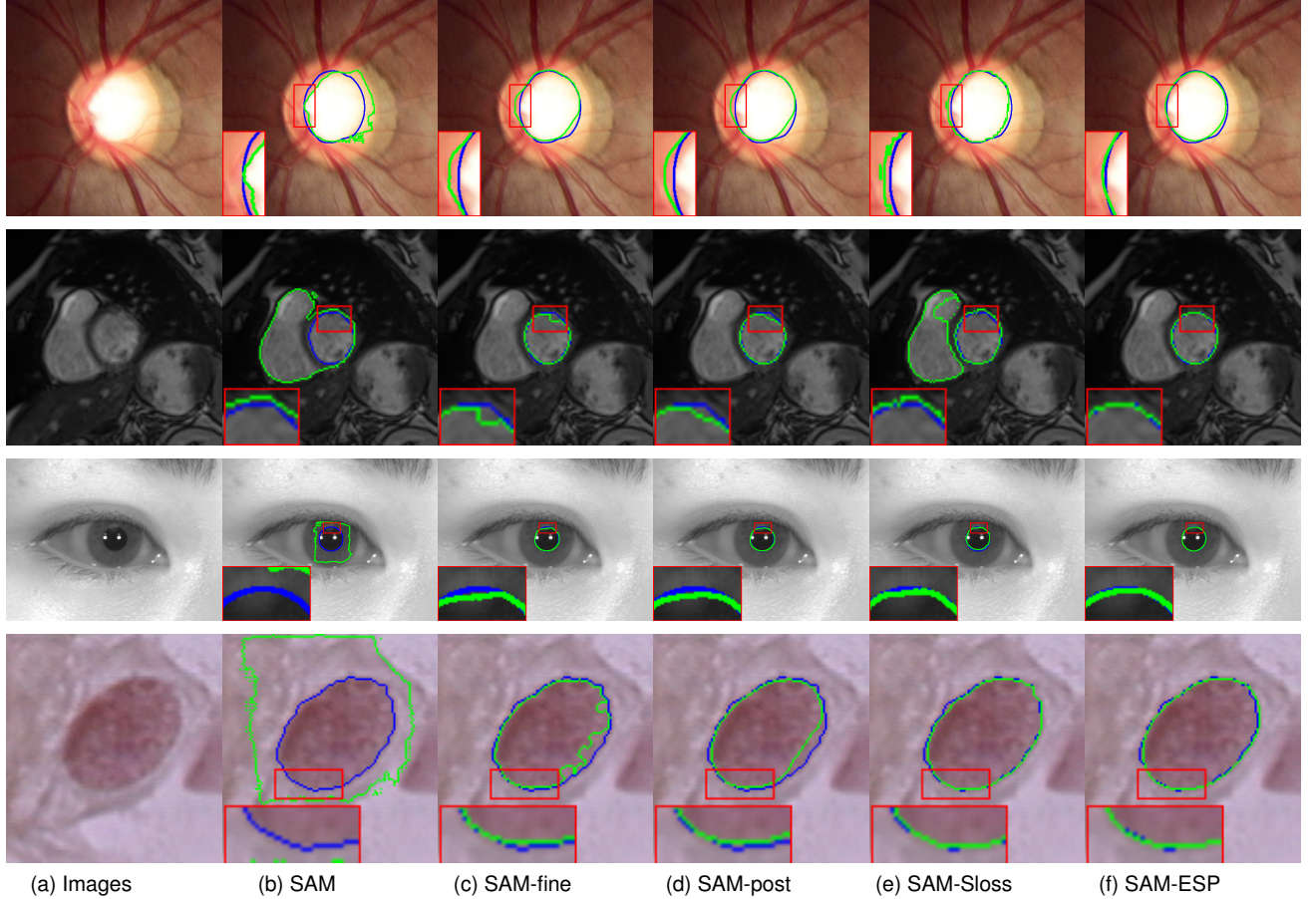


Figure 6: Visual effects of the segmentation results on four datasets. The blue line in the figure represents the segmentation contour of the ground truth, while the green line depicts the segmentation contours generated by various models. The red boxes indicate locally magnified views.

The initial SAM model, denoted as SAM, demonstrates suboptimal performance across all datasets, attributed to the inherent dissimilarity between these images and natural scenes. However, fine-tuning, denoted as SAM-fine, significantly improves segmentation accuracy and demonstrates that fine-tuning techniques can adapt models to specific domain information.

Furthermore, post-processing the segmentation outputs of SAM, termed SAM-post, yields enhancements, due to the predominant presence of elliptical shapes in our datasets. This refinement step contributes to more accurate delineation of object boundaries, aligning the segmentation results more closely with the expected shapes within the datasets.

Additionally, SAM-Sloss, which incorporates shape constraints into the loss function during model training, showcases improvements in segmentation accuracy. While not surpassing SAM-ESP’s performance, SAM-Sloss presents a notable advancement over the untuned SAM model and even the fine-tuned SAM in some instances. This suggests that leveraging shape constraints within the loss function can serve as a viable strategy for improving segmentation outcomes, although this method may not always exhibit stability.

Among all evaluated models, SAM-ESP emerges as the top performer, showcasing high segmentation accuracy across all metrics, particularly in terms of the Dice coefficient. SAM-ESP represents a novel approach where shape constraints are seamlessly integrated into the network architecture during model design. While SAM-Sloss and SAM-post exhibits commendable enhancements, SAM-ESP’s superior performance underscores its efficacy in preserving the elliptical shapes present in images. This innovative design choice proves instrumental in significantly enhancing segmentation accuracy, outperforming traditional post-processing techniques and loss function methods. For a more intuitive understanding, visual comparisons of the experimental outcomes are presented in Figure 6.

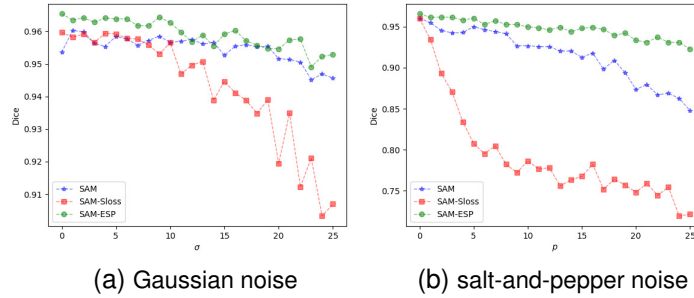


Figure 7: The generalization ability for different noise

Table 4: Test Results Under Noise Influence on DTU/Herlev Datasets

Noise	Network	Dice \uparrow	BD \downarrow	BDS \downarrow
GS	SAM-fine	95.12 \pm 0.54	2.07 \pm 0.17	2.20 \pm 0.17
	SAM-Sloss	93.13 \pm 0.18	2.56 \pm 0.06	2.14 \pm 0.15
	SAM-ESP	95.31\pm0.20	1.93\pm0.15	2.03\pm0.27
SP	SAM-fine	89.97 \pm 0.52	4.71 \pm 0.23	4.32 \pm 0.19
	SAM-Sloss	76.71 \pm 0.41	8.52 \pm 0.22	6.03 \pm 0.15
	SAM-ESP	93.75\pm1.07	2.51\pm0.32	2.34\pm0.34

*'GS' denotes the Gaussian noise while 'SP' denotes the salt-and-pepper noise.

6.6 Generalization Ability for Noise

To evaluate the generalization ability of ESP module under varying levels of noise, we introduced Gaussian noise with standard deviations (σ) ranging from 0 to 25 separately onto the DTU/Herlev test set. Additionally, to assess the model's robustness against different types of noise, we introduced salt-and-pepper noise (p) ranging from 0 to 25% of image pixels on the same test set. Figure 7a and Figure 7b respectively illustrate the Dice scores of three variants of the SAM model: SAM-fine, SAM trained with shape loss (SAM-Sloss), and SAM-ESP, under varying degrees of Gaussian and salt-and-pepper noise influences.

To facilitate comprehensive comparison across various metrics, we conducted a re-evaluation of the three models under specific conditions: a standard deviation of Gaussian noise set to 20 and 20% pixel contamination due to salt-and-pepper noise. The corresponding results are presented in Figure 8 and Table 4. From Figure 8, it can be observed that the addition of noise leads to less smooth boundaries in the segmentation results of SAM-fine. Particularly under the influence of salt-and-pepper noise, SAM-Sloss fails to correctly segment cell nuclei, whereas SAM-ESP maintains satisfactory segmentation results. Furthermore, from Figure 7, it is evident that as the intensity of noise increases, the segmentation accuracy of all three models begins to decline. Notably, SAM-Sloss exhibits a significant decrease in segmentation accuracy compared to the other two models, indicating pronounced sensitivity to noise. This sensitivity may stem from the shape prior in the loss function, which directs the model's focus more towards the current task during training at the expense of some generalization ability. Additionally, Figure 7 demonstrates that SAM-ESP consistently maintains higher segmentation accuracy under different noise conditions, with smaller declines in accuracy, particularly evident under salt-and-pepper noise interference. This stable performance underscores the superior robustness of SAM-ESP to noise interference.

6.7 Generalization Analysis on External Datasets

In this section, we evaluate the generalization capability of our models trained on the REFUGE dataset by testing them on two external datasets with distinct data distributions: RIM-ONE DL (Batista et al., 2020) and BinRushed (RIGA) (Almazroa et al., 2018; Eslami et al., 2023). The RIM-ONE DL dataset comprises 118 test images with optic cup masks from healthy subjects, while BinRushed contains 195 images with annotated optic cup and disc boundaries. All BinRushed images were center-cropped to 512 \times 512 for input standardization.

As demonstrated in Table 5, our SAM-ESP achieves superior performance on both external datasets (RIM-ONE DL and BinRushed) compared to the fine-tuned SAM baseline. These results indicate that SAM-ESP exhibits strong

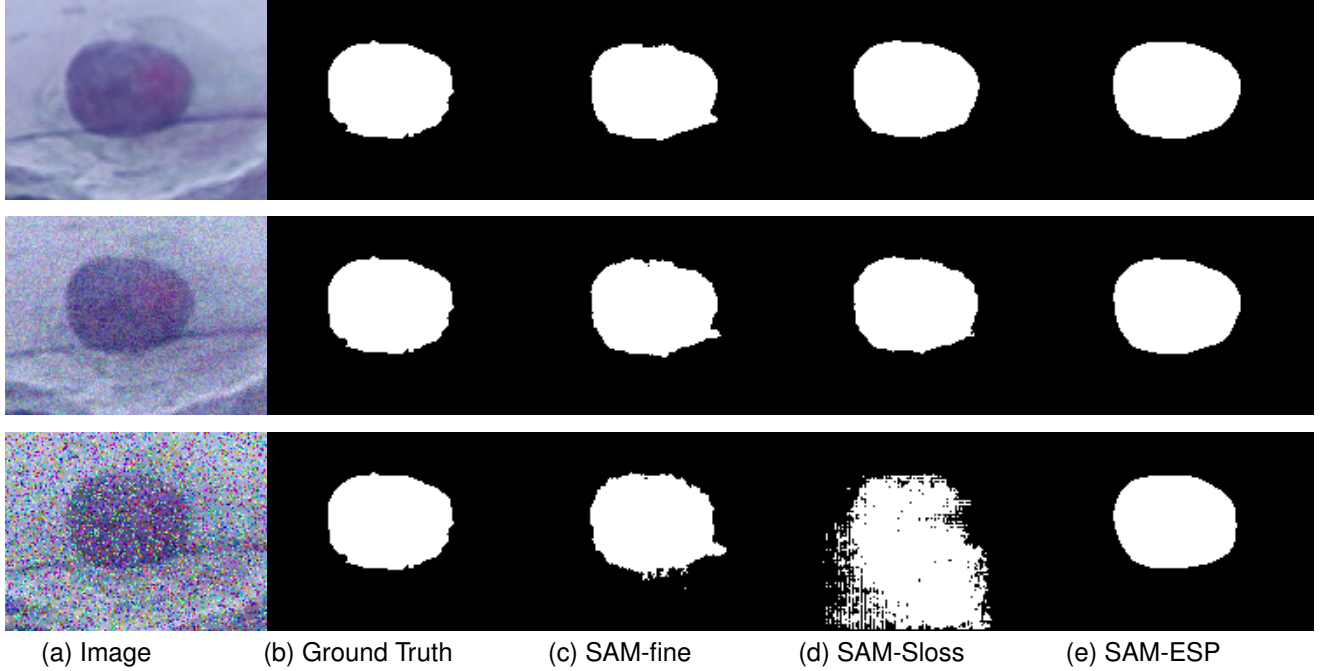


Figure 8: Visualization of model segmentation results under noise influence. The first row displays segmentation results without noise. The second row displays segmentation results under Gaussian noise with a standard deviation of 20, while the third row shows segmentation results under 20% salt-and-pepper noise.

Table 5: Test Results on External Datasets

Dataset	Network	Dice \uparrow	BD \downarrow	BDS \downarrow
RIM-ONE DL	SAM-fine	83.06 \pm 0.52	9.22 \pm 0.26	5.19 \pm 0.09
	SAM-Sloss	82.33 \pm 0.79	9.71 \pm 0.45	5.46 \pm 0.28
	SAM-ESP	83.68\pm0.41	8.78\pm0.14	4.96\pm0.05
BinRushed	SAM-fine	79.55 \pm 2.52	8.42 \pm 0.78	4.72 \pm 0.27
	SAM-Sloss	79.08 \pm 2.40	8.77 \pm 0.53	4.88 \pm 0.20
	SAM-ESP	80.51\pm2.84	7.45\pm0.50	4.17\pm0.21

cross-dataset generalization capability under varying data distributions. Moreover, the experimental results reveal that solely modifying the loss function degrades the model’s generalization ability. The qualitative results in Figure 9 confirm the advantages of our module in segmentation boundary accuracy.

6.8 Comparative Analysis

In this experimental section, we systematically compare the proposed method with three related state-of-the-art approaches on the REFUGE and ACDC datasets: Convex shape prior loss \mathcal{L}_{cs} (Han et al., 2020) enforces convexity constraints by penalizing cases where line segments between any two points within the segmented region fall outside the area; Ellipse fit error \mathcal{L}_{efe} (Akinlar et al., 2022) constrains geometric shapes by minimizing the distance between predicted segmentation boundaries and their best-fit ellipses; while Learnable Ophthalmology SAM (Qiu et al., 2023) incorporates learnable prompt layers into SAM’s encoder to enhance medical image adaptation. To ensure fair comparison, all methods follow the identical training-testing protocol: 100 epochs (LR=1e-4) for REFUGE and 50 epochs (LR=5e-5) for ACDC, with three independent runs per method. Test results are reported in Table 6. Some examples are also shown in Figure 10. From the experimental results, it can be seen that our SAM-ESP model better preserves the elliptical contour of the segmented region.

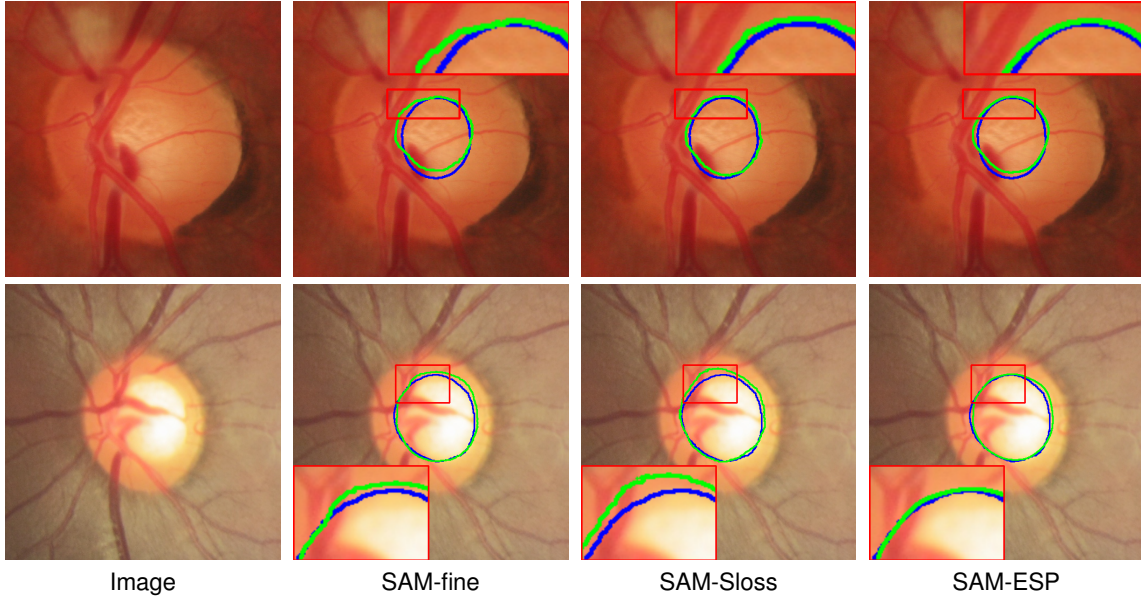


Figure 9: Visualization of segmentation results on external datasets. Blue: ground truth contours; green: model predictions. Red boxes highlight local details. The first row shows results on the RIM-ONE DL dataset, while the second row displays results on the BinRushed dataset.

Table 6: Comparative Experiments with the Most Related Methods

Method	Dice \uparrow	REFUGE	
		BD \downarrow	BDS \downarrow
SAMoph(Qiu et al., 2023)	84.54 \pm 0.10	9.49 \pm 0.14	5.60 \pm 0.09
SAM- \mathcal{L}_{cs} (Han et al., 2020)	87.00 \pm 0.54	7.75 \pm 0.37	4.47 \pm 0.18
SAM- \mathcal{L}_{efe} (Akinlar et al., 2022)	88.36 \pm 0.57	6.82 \pm 0.33	4.05 \pm 0.21
SAM-Sloss	88.78 \pm 0.15	6.67 \pm 0.08	3.87 \pm 0.07
SAM-ESP	89.07\pm0.14	6.36\pm0.11	3.75\pm0.13
Method	Dice \uparrow	ACDC	
		BD \downarrow	BDS \downarrow
SAMoph(Qiu et al., 2023)	92.98 \pm 0.48	1.28 \pm 0.18	0.93 \pm 0.03
SAM- \mathcal{L}_{cs} (Han et al., 2020)	95.20 \pm 0.08	0.87 \pm 0.006	0.81 \pm 0.02
SAM- \mathcal{L}_{efe} (Akinlar et al., 2022)	95.63 \pm 0.07	0.87 \pm 0.03	0.89 \pm 0.03
SAM-Sloss	95.51 \pm 0.20	0.86 \pm 0.03	0.90 \pm 0.03
SAM-ESP	95.85\pm0.09	0.76\pm0.004	0.78\pm0.01

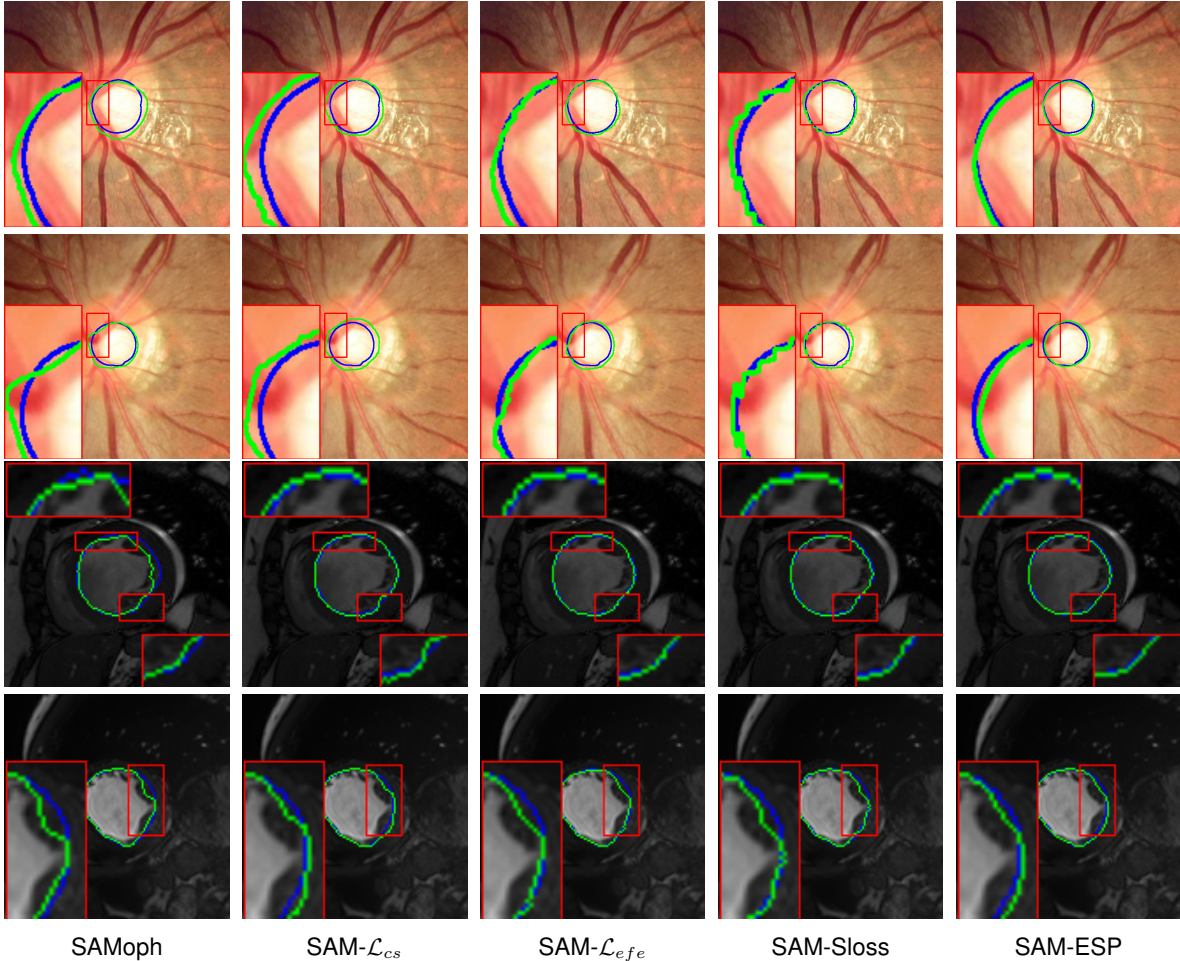


Figure 10: Segmentation results comparison. Blue: ground truth contours; green: model predictions. Red boxes highlight local details.

Table 7: Ablation Study on the Depths of ESP Module

ESP module	REFUGE		
	Dice \uparrow	BD \downarrow	BDS \downarrow
$T = 75$	88.34 \pm 0.07	6.79 \pm 0.10	3.99 \pm 0.07
$T = 100$	89.07\pm0.14	6.36\pm0.11	3.75\pm0.13
$T = 125$	88.05 \pm 0.51	7.16 \pm 0.34	4.20 \pm 0.15
$T = 150$	88.07 \pm 0.38	7.00 \pm 0.21	4.13 \pm 0.09

6.9 Ablation Study for ESP Module

In this section, we investigate the impact of different depths of the ESP module on segmentation performance. Specifically, we vary the number of algorithm iterations T , starting from $T = 75$ and increasing by 25 at each step. Experiments on the REFUGE dataset (Table 7) indicate that the best performance is achieved when $T = 100$. The ESP module is derived from our variational segmentation model, where each layer corresponds to one iteration of the algorithm. Thus, a sufficient number of iterations is required to achieve optimal results. However, during network training, computational complexity must also be considered, as excessively large T values may degrade the training process.

7 Conclusion

We have presented a novel segmentation algorithm that integrates an elliptical shape prior into the variational model through the constraint of the contour field. Our algorithm is rooted in the primal-dual theory, guaranteeing both stability and efficiency. The crucial sub-problem in our algorithm is the softmax, which allows for the integration of the elliptical shape, spatial regularization, and other priors in the model. This introduces a fresh perspective on incorporating elliptical priors into deep learning-based SAM image segmentation methods. Comparative results on different types of images showcase the robust performance of the proposed model in accurately segmenting elliptical regions.

Our method can be extended to any other deep neural network approaches for image segmentation. If the image segmentation dataset has an elliptical prior, our method can be used to construct an image segmentation deep network structure, ensuring that the network's output adheres to the elliptical shape prior.

Appendix A: Proof of Proposition 1

Proof. If the contours of $u(x, y)$ are ellipses, then $\exists \phi(t), \psi(t)$ defined by (13) such that $u(\phi(t), \psi(t)) = c$. Here c is a constant. Since u is \mathcal{C}^1 , differentiate both sides of the above equation with respect to t , we get $u_x \phi'(t) + u_y \psi'(t) = 0$, i.e. $\langle \nabla u(x, y), \mathbf{T}_\Lambda(x, y) \rangle = 0$.

Conversely, we prove by contradiction. Assume that when the conditions are satisfied, there is a contour of u is not ellipse. Denoting this contour as $u(x(t), y(t)) = c$, then we have $u_x x'(t) + u_y y'(t) = 0$. From the given conditions, we have the 2D vectors $(x'(t), y'(t))$ and $(\phi'(t), \psi'(t))$ are both orthogonal to ∇u , thus $(x'(t), y'(t))$ and $(\phi'(t), \psi'(t))$ are parallel. This implies that $(\phi(t), \psi(t))$ is not an ellipse. Contradiction! Therefore, the assumption is not valid, which completes the proof. \square

Appendix B: Calculation of \mathbf{u}^{t+1}

The subproblem of \mathbf{u} is:

$$\mathbf{u}^{t+1} = \arg \min_{\mathbf{u} \in \mathbb{U}} \{ \langle -\mathbf{o} + \mathbf{p}^t, \mathbf{u} \rangle + \varepsilon \langle \mathbf{u}, \ln(\mathbf{u}) \rangle + \langle \text{div}(q^{t+1} \mathbf{T}^t), \mathbf{u}_i \rangle \}.$$

For the simplicity of notation, let $\delta_{\hat{i}, i}$ be the delta function such that $\delta_{\hat{i}, i} = 1$ and $\delta_{\hat{i}, i} = 0, \hat{i} \neq i$ otherwise. We define $r_{\hat{i}} := -o_{\hat{i}} + p_{\hat{i}}^t + \delta_{\hat{i}, i} \text{div}(q^{t+1} \mathbf{T}^t)$ then the subproblem can be formulated as

$$\begin{aligned} \min_{\mathbf{u} \geq 0} & \left\{ \sum_{\hat{i}=1}^I \int_{\Omega} r_{\hat{i}}(x) u_{\hat{i}}(x) dx + \int_{\Omega} \varepsilon u_{\hat{i}}(x) \ln u_{\hat{i}}(x) dx \right\} \\ \text{s.t.} & \sum_{\hat{i}=1}^I u_{\hat{i}}(x) = 1, \quad \forall x \in \Omega. \end{aligned}$$

By introducing Lagrangian multiplier v associated to the constraint $\sum_{\hat{i}=1}^I u_{\hat{i}}(x) = 1, \forall x \in \Omega$, we have the related

Lagrangian function:

$$\begin{aligned} \mathcal{L}(\mathbf{u}, v) &= \sum_{\hat{i}=1}^I \int_{\Omega} r_{\hat{i}}(x) u_{\hat{i}}(x) dx + \sum_{\hat{i}=1}^I \int_{\Omega} \varepsilon u_{\hat{i}}(x) \ln u_{\hat{i}}(x) dx \\ &+ \int_{\Omega} v(x) \left(1 - \sum_{\hat{i}=1}^I u_{\hat{i}}(x) \right) dx. \end{aligned}$$

The variation of \mathcal{L} with respect to $u_{\hat{i}}$:

$$\frac{\partial \mathcal{L}}{\partial u_{\hat{i}}} = r_{\hat{i}} + \varepsilon \ln u_{\hat{i}} + \varepsilon - v = 0.$$

therefore, by the first order optimization condition, we have

$$u_{\hat{i}}^{t+1}(x) = e^{\frac{-r_{\hat{i}}(x) + v(x)}{\varepsilon}} - 1,$$

Table 8: Test Results based on Other Model

Class	Network	Dice \uparrow	BD \downarrow	BDS \downarrow
pupil	Unet++	94.19 \pm 0.42	7.97 \pm 2.36	10.24 \pm 3.14
	+ESP	94.57\pm0.06	2.82\pm0.91	3.21\pm1.93
iris	Unet++	95.36 \pm 0.13	8.75 \pm 1.78	11.99 \pm 1.78
	+ESP	95.43\pm0.18	6.53\pm1.10	8.65\pm1.61

Furthermore, sum both sides of the equation and use the constraint condition, one can obtain

$$1 = \sum_{\hat{i}=1}^I u_{\hat{i}}(x) = e^{\frac{v(x)}{\varepsilon}} - 1 \sum_{\hat{i}=1}^I e^{\frac{-r_{\hat{i}}(x)}{\varepsilon}},$$

Substitute the above expression back into the expression for $u_{\hat{i}}^{t+1}$, finally we obtain

$$u_{\hat{i}}^{t+1} = \frac{e^{\frac{-r_{\hat{i}}}{\varepsilon}}}{\sum_{i'=1}^I e^{\frac{-r_{i'}}{\varepsilon}}} = \frac{e^{\frac{\sigma_{\hat{i}} - p_{\hat{i}}^t - \delta_{\hat{i}, \hat{i}} \operatorname{div}(q^{t+1} \mathbf{T}^t)}{\varepsilon}}}{\sum_{i'=1}^I e^{\frac{\sigma_{i'} - p_{i'}^t - \delta_{i', i'} \operatorname{div}(q^{t+1} \mathbf{T}^t)}{\varepsilon}}}, \quad \hat{i} = 1, \dots, I.$$

Appendix C: Experiments based on other models

In this section, we conduct experiments using Unet++ as baseline models to validate the effectiveness of the proposed Ellipse Shape Prior (ESP) module on the CASIA.v4 dataset. The network is trained to simultaneously segment both pupil and iris regions, with unified ellipse shape constraints applied to these two elliptical structures. Quantitative results presented in Table 8 demonstrate that incorporating the ESP module improves the Dice scores for both categories, with particularly significant enhancements in boundary accuracy metrics BD and BDS. Qualitative results illustrated in Figure. 11 further confirm the module’s capability to enhance the segmentation of elliptical structures.

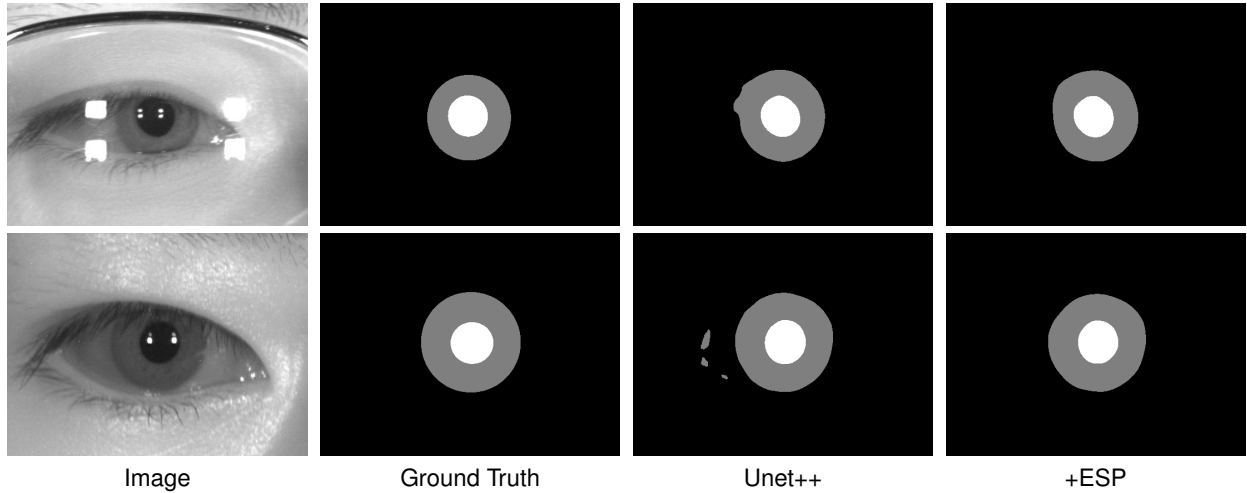


Figure 11: Visualization of segmentation results on CASIA.v4 datasets

References

- Renfrey Burnard Potts. Some generalized order-disorder transformations. In *Math. Proc. Cambridge Philos. Soc.*, volume 48, pages 106–109. Cambridge University Press, 1952.
- Michael Kass, Andrew Witkin, and Demetri Terzopoulos. Snakes: Active contour models. *Int. J. Comput. Vis.*, 1(4): 321–331, January 1987. ISSN 1573-1405.

- Tony F Chan and Luminita A Vese. Active contours without edges. *IEEE Trans. Image Process.*, 10(2):266–277, February 2001. ISSN 1941-0042.
- Yuri Y Boykov and M-P Jolly. Interactive graph cuts for optimal boundary & region segmentation of objects in N-D images. In *Proc. 8th IEEE Int. Conf. Comput. Vision. (ICCV)*, volume 1, pages 105–112, July 2001.
- Piali Das, Olga Veksler, Vyacheslav Zavadsky, and Yuri Boykov. Semiautomatic segmentation with compact shape prior. *Image Vis. Comput.*, 27(1-2):206–219, 2009.
- Sara Vicente, Vladimir Kolmogorov, and Carsten Rother. Graph cut based image segmentation with connectivity priors. In *Proc. IEEE Conf. Comput. Vis. Pattern Recognit.*, pages 1–8, June 2008.
- Olga Veksler. Star shape prior for graph-cut image segmentation. In *Proc. 10th Eur. Conf. Comput. Vis.*, pages 454–467, Oct 2008.
- Lena Gorelick, Olga Veksler, Yuri Boykov, and Claudia Nieuwenhuis. Convexity shape prior for binary segmentation. *IEEE Trans. Pattern Anal. Mach. Intell.*, 39(2):258–271, February 2017.
- Shi Yan, Xue-Cheng Tai, Jun Liu, and Hai-Yang Huang. Convexity shape prior for level set-based image segmentation method. *IEEE Trans. Image Process.*, 29:7141–7152, June 2020.
- Hai-Shan Wu, J. Barba, and J. Gil. A parametric fitting algorithm for segmentation of cell images. *IEEE Trans. Biomed. Eng.*, 45(3):400–407, March 1998. doi:10.1109/10.661165.
- Shu-Hung Leung, Shi-Lin Wang, and Wing-Hong Lau. Lip image segmentation using fuzzy clustering incorporating an elliptic shape function. *IEEE Trans. Image Process.*, 13(1):51–62, January 2004. doi:10.1109/TIP.2003.818116.
- Greg Slabaugh and Gozde Unal. Graph cuts segmentation using an elliptical shape prior. In *Proc. IEEE Int. Conf. Image Process. (ICIP)*, volume 2, pages 1222–1225, September 2005.
- Ujjwal Verma, Florence Rossant, Isabelle Bloch, Julien Orensanz, and Denis Boissongtier. Shape-based segmentation of tomatoes for agriculture monitoring. In *Proc. 3rd Int. Conf. Pattern Recognit. Appl. Methods (ICPRAM)*, pages 402–411, March 2014.
- Charles O. Ukpai, Satnam S. Dlay, and Wai L. Woo. Pupil segmentation using active contour with shape prior. In *Sixth International Conference on Graphic and Image Processing (ICGIP 2014)*, volume 9443, pages 566–570, October 2014. doi:10.1117/12.2180065.
- Yuwei Wu, Yuanquan Wang, and Yunde Jia. Segmentation of the left ventricle in cardiac cine MRI using a shape-constrained snake model. *Comput. Vis. Image Underst.*, 117(9):990–1003, September 2013. ISSN 1077-3142. doi:https://doi.org/10.1016/j.cviu.2012.12.008.
- Evan Shelhamer, Jonathan Long, and Trevor Darrell. Fully convolutional networks for semantic segmentation. *IEEE Trans. Pattern Anal. Mach. Intell.*, 39(4):640–651, April 2017. doi:10.1109/TPAMI.2016.2572683.
- Olaf Ronneberger, Philipp Fischer, and Thomas Brox. U-Net: Convolutional networks for biomedical image segmentation. In *Proc. 18th Int. Conf. Med. Image Comput. Comput.-Assist. Intervent. (MICCAI)*, pages 234–241, May 2015.
- Alexander Kirillov et al. Segment anything. In *Proc. IEEE/CVF Conf. Comput. Vis.*, pages 4015–4026, Oct 2023.
- Jun Ma, Yuting He, Feifei Li, Lin Han, Chenyu You, and Bo Wang. Segment anything in medical images. *Nat. Commun.*, 15(1):654, January 2024. ISSN 2041-1723. doi:10.1038/s41467-024-44824-z.
- Xinrong Hu, Xiaowei Xu, and Yiyu Shi. How to efficiently adapt large segmentation model(SAM) to medical images, June 2023. URL <http://arxiv.org/abs/2306.13731>. arXiv:2306.13731.
- Junlong Cheng et al. SAM-Med2D, August 2023. URL <https://arxiv.org/abs/2308.16184v1>. arXiv:2308.16184.
- Zhongxi Qiu, Yan Hu, Heng Li, and Jiang Liu. Learnable ophthalmology SAM, April 2023. URL <http://arxiv.org/abs/2304.13425>. arXiv:2304.13425.
- Jie Zhang, Xubing Yang, Rui Jiang, Wei Shao, and Li Zhang. RSAM-Seg: A SAM-based approach with prior knowledge integration for remote sensing image semantic segmentation, February 2024. URL <http://arxiv.org/abs/2402.19004>. arXiv:2402.19004.
- Tianrun Chen et al. SAM fails to segment anything? – SAM-Adapter: Adapting SAM in underperformed scenes: camouflage, shadow, medical image segmentation, and more, May 2023. URL <http://arxiv.org/abs/2304.09148>. arXiv:2304.09148.
- Zahra Mirikharaji and Ghassan Hamarneh. Star shape prior in fully convolutional networks for skin lesion segmentation. In *Proc. Int. Conf. Med. Image Comput. Comput.-Assist. Intervent.*, pages 737–745, June 2018.

- Sang Yoon Han, Hyuk Jin Kwon, Yoonsik Kim, and Nam Ik Cho. Noise-robust pupil center detection through cnn-based segmentation with shape-prior loss. *IEEE Access*, 8:64739–64749, April 2020. doi:10.1109/ACCESS.2020.2985095.
- Cuneyt Akinlar, Hatice Kubra Kucukkartal, and Cihan Topal. Accurate cnn-based pupil segmentation with an ellipse fit error regularization term. *Expert Syst. Appl.*, 188:116004, February 2022. ISSN 0957-4174. doi:<https://doi.org/10.1016/j.eswa.2021.116004>.
- Jun Liu, Xiangyue Wang, and Xue-Cheng Tai. Deep convolutional neural networks with spatial regularization, volume and star-shape priors for image segmentation. *J. Math. Imaging Vis.*, 64(6):625–645, Jul 2022. ISSN 0924-9907. doi:10.1007/s10851-022-01087-x.
- Shengzhe Chen, Zhaoxuan Dong, and Jun Liu. Contour flow constraint: Preserving global shape similarity for deep learning based image segmentation, 2025. URL <https://arxiv.org/abs/2504.09384>. arXiv:2504.09384.
- Jing Yuan, Egil Bae, Xue-Cheng Tai, and Yuri Boykov. A continuous max-flow approach to potts model. In Kostas Daniilidis, Petros Maragos, and Nikos Paragios, editors, *Computer Vision – ECCV 2010*, pages 379–392, Berlin, Heidelberg, 2010. Springer Berlin Heidelberg. ISBN 978-3-642-15567-3.
- Selim Esedoğ Lu and Felix Otto. Threshold dynamics for networks with arbitrary surface tensions. *Commun. Pure Appl. Math.*, 68(5):808–864, May 2015.
- Dong Wang, Haohan Li, Xiaoyu Wei, and Xiao-Ping Wang. An efficient iterative thresholding method for image segmentation. *J. Comput. Phys.*, 350:657–667, Dec 2017. ISSN 0021-9991.
- Alexey Dosovitskiy et al. An image is worth 16x16 words: transformers for image recognition at scale, June 2021. URL <http://arxiv.org/abs/2010.11929>. arXiv:2010.11929.
- Chaoning Zhang et al. Understanding segment anything model: SAM is biased towards texture rather than shape, June 2023. URL <http://arxiv.org/abs/2311.11465>. arXiv:2311.11465.
- José Ignacio Orlando et al. Refuge challenge: A unified framework for evaluating automated methods for glaucoma assessment from fundus photographs. *Med. Image Anal.*, 59:101570, January 2020. ISSN 1361-8415. doi:10.1016/j.media.2019.101570.
- Olivier Bernard et al. Deep learning techniques for automatic MRI cardiac multi-structures segmentation and diagnosis: Is the problem solved? *IEEE Trans. Med. Imag.*, 37(11):2514–2525, November 2018. doi:10.1109/TMI.2018.2837502.
- B. I. Test. Casia iris database v4. [Online]. Available: <http://www.idealtest.org/dbDetailForUser.do?id=4#/>.
- Caiyong Wang, Jawad Muhammad, Yunlong Wang, Zhaofeng He, and Zhenan Sun. Towards complete and accurate iris segmentation using deep multi-task attention network for non-cooperative iris recognition. *IEEE Trans. Inf. Forensics Secur.*, 15:2944–2959, March 2020.
- Jan Jantzen, Jonas Norup, Georgios Dounias, and Beth Bjerregaard. Pap-smear benchmark data for pattern classification. In *Proc. Nature Inspired Smart Inf. Syst. (NiSIS)*, pages 1–9, January 2005.
- Francisco José Fumero Batista, Tinguaro Diaz-Aleman, Jose Sigut, Silvia Alayon, Rafael Arnay, and Denisse Angel-Pereira. Rim-one dl: A unified retinal image database for assessing glaucoma using deep learning. *Image Anal. Stereol.*, 39(3):161–167, November 2020. ISSN 1854-5165.
- Ahmed Almazroa, Sami Alodhayb, Essameldin Osman, Eslam Ramadan, Mohammed Hummadi, Mohammed Dlaim, Muhannad Alkatee, Kaamran Raahemifar, and Vasudevan Lakshminarayanan. Retinal fundus images for glaucoma analysis: the riga dataset. In *Proc. SPIE, Med. Imag., Imag. Informat. Healthcare, Res., Appl.*, volume 10579, pages 55–62. SPIE, March 2018. doi:10.1117/12.2293584.
- Mohammad Eslami, Lakshmi Sritan Motati, Rohan Kalahasty, Saber Kazeminasab Hashemabad, Min Shi, Yan Luo, Yu Tian, Nazlee Zebardast, Mengyu Wang, and Tobias Elze. Deep learning based adversarial disturbances in fundus image analysis. *Investigative Ophthalmology & Visual Science*, 64(9):PB002–PB002, June 2023.